

Optical design of organic solar cell with hybrid plasmonic system

Wei E. I. Sha,¹ Wallace C. H. Choy,¹ Yongpin P. Chen,¹ and
Weng Cho Chew^{1,2,*}

¹*Department of Electrical and Electronic Engineering, The University of Hong Kong,
Pokfulam Road, Hong Kong*

²*Department of Electrical and Computer Engineering, University of Illinois,
Urbana-Champaign, Illinois, USA*

[*wcc Chew@hku.hk](mailto:wcc Chew@hku.hk)

Abstract: We propose a novel optical design of organic solar cell with a hybrid plasmonic system, which comprises a plasmonic cavity coupled with a dielectric core-metal shell nanosphere. From a rigorous solution of Maxwell's equations, called volume integral equation method, optical absorption of the active polymer material has a four-fold increase. The significant enhancement mainly attributes to the coupling of symmetric surface wave modes supported by the cavity resonator. The dispersion relation of the plasmonic cavity is characterized by solving an 1D eigenvalue problem of the air/metal/polymer/metal/air structure with finite thicknesses of metal layers. We demonstrate that the optical enhancement strongly depends on the decay length of surface plasmon waves penetrated into the active material. Furthermore, the coherent interplay between the cavity and the dielectric core-metal shell nanosphere is undoubtedly confirmed by our theoretical model. The work offers detailed physical explanations to the hybrid plasmonic cavity device structure for enhancing the optical absorption of organic photovoltaics.

© 2011 Optical Society of America

OCIS codes: (310.6628) Subwavelength structures, nanostructures; (040.5350) Photovoltaic; (250.5403) Plasmonics; (050.1755) Computational electromagnetic methods.

References and links

1. K. L. Chopra, P. D. Paulson, and V. Dutta, "Thin-film solar cells: an overview," *Prog. Photovoltaics* **12**, 69–92 (2004).
2. H. Hoppe and N. S. Sariciftci, "Organic solar cells: an overview," *J. Mater. Res.* **19**, 1924–1945 (2004).
3. R. A. Pala, J. White, E. Barnard, J. Liu, and M. L. Brongersma, "Design of plasmonic thin-film solar cells with broadband absorption enhancements," *Adv. Mater.* **21**, 3504–3509 (2009).
4. W. E. I. Sha, W. C. H. Choy, and W. C. Chew, "A comprehensive study for the plasmonic thin-film solar cell with periodic structure," *Opt. Express* **18**, 5993–6007 (2010).
5. W. L. Barnes, A. Dereux, and T. W. Ebbesen, "Surface plasmon subwavelength optics," *Nature* **424**, 824–830 (2003).
6. J. A. Schuller, E. S. Barnard, W. S. Cai, Y. C. Jun, J. S. White, and M. L. Brongersma, "Plasmonics for extreme light concentration and manipulation," *Nat. Mater.* **9**, 193–204 (2010).
7. S. A. Maier, *Plasmonics: Fundamentals and Applications* (Springer, 2007).
8. H. A. Atwater and A. Polman, "Plasmonics for improved photovoltaic devices," *Nat. Mater.* **9**, 205–213 (2010).
9. A. J. Morfa, K. L. Rowlen, T. H. Reilly, M. J. Romero, and J. van de Lagemaat, "Plasmon-enhanced solar energy conversion in organic bulk heterojunction photovoltaics," *Appl. Phys. Lett.* **92**, 013504 (2008).
10. W. L. Bai, Q. Q. Gan, G. F. Song, L. H. Chen, Z. Kafafi, and F. Bartoli, "Broadband short-range surface plasmon structures for absorption enhancement in organic photovoltaics," *Opt. Express* **18**, A620–A630 (2010).

11. M. G. Kang, T. Xu, H. J. Park, X. G. Luo, and L. J. Guo, "Efficiency enhancement of organic solar cells using transparent plasmonic Ag nanowire electrodes," *Adv. Mater.* **22**, 4378–4383 (2010).
12. C. J. Min, J. Li, G. Veronis, J. Y. Lee, S. H. Fan, and P. Peumans, "Enhancement of optical absorption in thin-film organic solar cells through the excitation of plasmonic modes in metallic gratings," *Appl. Phys. Lett.* **96**, 133302 (2010).
13. W. E. I. Sha, W. C. H. Choy, and W. C. Chew, "Angular response of thin-film organic solar cells with periodic metal back nanostrips," *Opt. Lett.* **36**, 478–480 (2011).
14. D. Duche, P. Torchio, L. Escoubas, F. Monestier, J. J. Simon, F. Flory, and G. Mathian, "Improving light absorption in organic solar cells by plasmonic contribution," *Sol. Energy Mater. Sol. Cells* **93**, 1377–1382 (2009).
15. J. Jung, T. G. Pedersen, T. Sondergaard, K. Pedersen, A. N. Larsen, and B. B. Nielsen, "Electrostatic plasmon resonances of metal nanospheres in layered geometries," *Phys. Rev. B* **81**, 125413 (2010).
16. S. J. Tsai, M. Ballarotto, D. B. Romero, W. N. Herman, H. C. Kan, and R. J. Phaneuf, "Effect of gold nanopillar arrays on the absorption spectrum of a bulk heterojunction organic solar cell," *Opt. Express* **18**, A528–A535 (2010).
17. I. Diukman, L. Tzabari, N. Berkovitch, N. Tessler, and M. Orenstein, "Controlling absorption enhancement in organic photovoltaic cells by patterning Au nano disks within the active layer," *Opt. Express* **19**, A64–A71 (2011).
18. J. Jung, T. Sondergaard, T. G. Pedersen, K. Pedersen, A. N. Larsen, and B. B. Nielsen, "Dyadic Green's functions of thin films: Applications within plasmonic solar cells," *Phys. Rev. B* **83**, 085419 (2011).
19. V. E. Ferry, L. A. Sweatlock, D. Pacifici, and H. A. Atwater, "Plasmonic nanostructure design for efficient light coupling into solar cells," *Nano Lett.* **8**, 4391–4397 (2008).
20. B. T. Draine and P. J. Flatau, "Discrete-dipole approximation for scattering calculations," *J. Opt. Soc. Am. A* **11**, 1491–1499 (1994).
21. A. M. Kern and O. J. F. Martin, "Surface integral formulation for 3D simulations of plasmonic and high permittivity nanostructures," *J. Opt. Soc. Am. A* **26**, 732–740 (2009).
22. A. W. Glisson and D. R. Wilton, "Simple and efficient numerical methods for problems of electromagnetic radiation and scattering from surfaces," *IEEE Trans. Antennas Propag.* **28**, 593–603 (1980).
23. M. F. Catedra, E. Gago, and L. Nuno, "A numerical scheme to obtain the RCS of three-dimensional bodies of resonant size using the conjugate gradient method and the fast Fourier transform," *IEEE Trans. Antennas Propag.* **37**, 528–537 (1989).
24. H. A. Vandervorst, "Bi-CGSTAB: A fast and smoothly converging variant of Bi-CG for the solution of nonsymmetric linear systems," *SIAM J. Sci. Stat. Comput.* **13**, 631–644 (1992).
25. W. C. H. Choy and H. H. Fong, "Comprehensive investigation of absolute optical properties of organic materials," *J. Phys. D: Appl. Phys.* **41**, 155109 (2008).
26. A. D. Rakic, A. B. Djuricic, J. M. Elazar, and M. L. Majewski, "Optical properties of metallic films for vertical-cavity optoelectronic devices," *Appl. Opt.* **37**, 5271–5283 (1998).
27. E. D. Palik, *Handbook of Optical Constants of Solids* (Academic Press, 1998).
28. E. Prodan, C. Radloff, N. J. Halas, and P. Nordlander, "A hybridization model for the plasmon response of complex nanostructures," *Science* **302**, 419–422 (2003).
29. W. C. Chew, *Waves and Fields in Inhomogeneous Media* (Wiley-IEEE Press, 1999).
30. L. Tsang, J. A. Kong, and K. H. Ding, *Scattering of Electromagnetic Waves: Theories and Applications* (Wiley, 2000).
31. B. Prade, J. Y. Vinet, and A. Mysyrowicz, "Guided optical waves in planar heterostructures with negative dielectric-constant," *Phys. Rev. B* **44**, 13556–13572 (1991).
32. J. P. Berenger, "A perfectly matched layer for the absorption of electromagnetic-waves," *J. Comput. Phys.* **114**, 185–200 (1994).
33. W. C. Chew and W. H. Weedon, "A 3-D perfectly matched medium from modified Maxwell's equations with stretched coordinates," *Microw. Opt. Technol. Lett.* **7**, 599–604 (1994).

1. Introduction

Critically different from the thin-film polycrystalline or amorphous silicon solar cells (SCs) with active layer thickness of a few microns [1], the active polymer layer of thin-film organic solar cells (OSCs) only has few hundreds nanometers or even thinner thickness due to an extreme short exciton diffusion length [2]. Such thin active layer with low refractive index ($n \approx 1.8$) induces not only the weak optical absorption of OSCs but also fundamental (half-wavelength) limits of the optical design. On one hand, the strong Fabry-Pérot photonic mode or waveguide mode [3, 4] cannot be expected in the ultra-thin active layer. On the other hand, the physical mechanism of near-field concentration (not far-field scattering) should be taken

into account in the design. Having unique features of tunable subwavelength resonance and engineered near-field concentration, plasmon is an enabling technique for light manipulation and management [5–7]. Plasmonic effects allow us to unprecedentedly improve the optical absorption of thin-film OSCs [8] and promote emerging SC technology meeting clean energy demands. Plasmonic nanostructures can offer three principles to enhance the optical absorption of OSCs. The first one is surface plasmon resonance by metal gratings fabricated on the top or bottom of the active layer [9–13]. The second one is local plasmon resonance by metal particles incorporated into or near the active layer [14–18]. The third one is plasmon coupling and hybridization, such as surface plasmon resonance coupled with local plasmon resonance or plasmon resonance coupled with photonic resonance [19].

In the paper, we propose a novel optical design of OSC with a hybrid plasmonic system, which comprises a plasmonic cavity coupled with a dielectric core-metal shell nanosphere. It has been investigated that optical absorption of the active polymer material has a four-fold increase. With the help of rigorous electrodynamic approaches, we unveil the fundamental physics of the significant enhancement, which mainly attributes to the coupling of symmetric surface wave modes supported by the cavity resonator with a long penetration length. Moreover, coherent interaction between the cavity and the dielectric core-metal shell nanosphere is definitely confirmed by our theoretical model. A distribution of polarization charges on the surface of the cavity indicates a bonding and antibonding coupling modes in the hybrid plasmonic system. The work introduces a new hybrid plasmonic cavity device structure to enhance the optical absorption of organic photovoltaics with detailed physical explanations.

2. Theoretical Model

As a rigorous solution to Maxwell's equations, a volume integral equation (VIE) method is developed to characterize the optical absorption of OSCs. Considering non-magnetic optical materials with an arbitrary inhomogeneity profile, the VIE can be written as

$$\mathbf{E}^i(\mathbf{r}) = \frac{\mathbf{J}(\mathbf{r})}{-i_0\omega(\varepsilon(\mathbf{r}) - \varepsilon_0)} - i_0\omega\mu_0 \int_v \overline{\mathbf{G}}(\mathbf{r}, \mathbf{r}') \cdot \mathbf{J}(\mathbf{r}') d\mathbf{r}' \quad (1)$$

where i_0 is the imaginary unit, ε_0 (μ_0) is the permittivity (permeability) of free space, $\mathbf{E}^i(\mathbf{r})$ is the incident electric field of the light, $\varepsilon(\mathbf{r})$ is the position-dependent permittivity of the inhomogeneous materials, \mathbf{J} is the volumetric polarization current to be solved, and $\overline{\mathbf{G}}(\mathbf{r}, \mathbf{r}')$ is the dyadic Green's tensor in free space. The widely adopted approach for solving the VIE is the discrete dipole approximation (DDA) method [20]. Due to the hypersingularity of the Green's tensor and spurious discontinuity of tangential E -field induced by the scalar (piecewise constant) basis functions, the DDA method cannot accurately characterize the subwavelength plasmonic physics [21] and breaks down in the multilayer device structure with high-contrast metallic materials. Here, we develop an alternate algorithm to bypass the difficulties. In our model, the polarization currents are expanded using the roof-top vector basis functions [22] and thus the continuity of normal current is naturally satisfied at the material interfaces. Furthermore, the hypersingular Green's tensor is smoothed by using the finite-difference approximation.

From the VIE [Eq. (1)], the scattered electric field generated by the volumetric polarization current \mathbf{J} can be written as

$$\mathbf{E}^s(\mathbf{r}) = i_0\omega\mu_0 \int_v \overline{\mathbf{G}}(\mathbf{r}, \mathbf{r}') \cdot \mathbf{J}(\mathbf{r}') d\mathbf{r}' \quad (2)$$

Considering the Cartesian coordinate system, we use the short notation (u_1, u_2, u_3) substituting

for (x, y, z) , then we have

$$\begin{bmatrix} E_1^s \\ E_2^s \\ E_3^s \end{bmatrix} = \begin{bmatrix} L_{11} & L_{12} & L_{13} \\ L_{21} & L_{22} & L_{23} \\ L_{31} & L_{32} & L_{33} \end{bmatrix} \begin{bmatrix} J_1 \\ J_2 \\ J_3 \end{bmatrix} \quad (3)$$

where

$$L_{ij} = \begin{cases} L_{ii}^c + L_{ii}^q, & i = j \\ L_{ij}^q, & i \neq j \end{cases} \quad (4)$$

$$L_{ii}^c J_i = i_0 \omega \mu_0 \int_V g(\mathbf{r}, \mathbf{r}') J_i(\mathbf{r}') d\mathbf{r}' \quad (5)$$

$$L_{ij}^q J_j = \frac{i_0}{\omega \epsilon_0} \frac{\partial}{\partial u_i} \int_V g(\mathbf{r}, \mathbf{r}') \frac{\partial J_j(\mathbf{r}')}{\partial u_j'} d\mathbf{r}' \quad (6)$$

where $g(\mathbf{r}, \mathbf{r}') = \frac{\exp(i_0 K_0 |\mathbf{r} - \mathbf{r}'|)}{4\pi |\mathbf{r} - \mathbf{r}'|}$ is the scalar green's function, $\bar{\mathbf{G}}(\mathbf{r}, \mathbf{r}') = \left[\bar{\mathbf{I}} + \frac{\nabla \nabla}{K_0^2} \right] g(\mathbf{r}, \mathbf{r}')$, and K_0 is the wave number of free space.

Using the rooftop basis functions to expand the unknown currents, we have

$$\mathbf{J}(\mathbf{r}) = \sum_{i=1}^3 \mathbf{u}_i \sum_{k,m,n} J_i^D(k, m, n) T_{k,m,n}^i \quad (7)$$

where $T_{k,m,n}^1$, $T_{k,m,n}^2$, and $T_{k,m,n}^3$ are the volumetric rooftop functions given by

$$\begin{aligned} T_{k,m,n}^1 &= \Lambda_k(u_1) \Pi_m(u_2) \Pi_n(u_3) \\ T_{k,m,n}^2 &= \Pi_k(u_1) \Lambda_m(u_2) \Pi_n(u_3) \\ T_{k,m,n}^3 &= \Pi_k(u_1) \Pi_m(u_2) \Lambda_n(u_3) \end{aligned} \quad (8)$$

The functions $\Lambda_k(u_1)$ and $\Pi_m(u_2)$ are defined by

$$\begin{aligned} \Lambda_k(u_1) &= \begin{cases} 1 - \frac{|u_1 - k\Delta u_1|}{\Delta u_1}, & |u_1 - k\Delta u_1| \leq \Delta u_1 \\ 0, & \text{else} \end{cases} \\ \Pi_m(u_2) &= \begin{cases} 1, & \left| u_2 - \left(m - \frac{1}{2} \right) \Delta u_2 \right| < \frac{\Delta u_2}{2} \\ 0, & \text{else} \end{cases} \end{aligned} \quad (9)$$

The cuboid cells are employed to discretize the structure to be modeled. Here, Δu_1 and Δu_2 are the grid sizes of each small cuboid along x and y directions, respectively. Other functions in Eq. (8) can be defined in the same way.

As a result, the discretized form for the operator L_{ii}^c in Eq. (5) can be written as

$$L_{ii}^{D,c} J_i^D = i_0 \omega \mu_0 g^D \otimes J_i^D \quad (10)$$

where \otimes denotes the discrete convolution

$$g^D \otimes J_i^D = \sum_{k,m,n} g^D(k - k', m - m', n - n') J_i^D(k', m', n') \quad (11)$$

and

$$g^D(k, m, n) = \int_0^{\Delta u_1} \int_0^{\Delta u_2} \int_0^{\Delta u_3} g(u_{1,k} - u'_1, u_{2,m} - u'_2, u_{3,n} - u'_3) du'_1 du'_2 du'_3 \quad (12)$$

Likewise, the operator $L_{12}^{D,q}$ in Eq. (6) can be discretized as

$$\begin{aligned} L_{12}^{D,q} J_2^D &= \frac{i_0}{\omega \epsilon_0 \Delta u_1 \Delta u_2} [g^D(k+1, m, n) - g^D(k, m, n)] \otimes [J_2^D(k, m, n) - J_2^D(k, m-1, n)] \\ &= \frac{i_0}{\omega \epsilon_0 \Delta u_1 \Delta u_2} \{ [g^D(k+1, m, n) - g^D(k, m, n)] - \\ &\quad [g^D(k+1, m-1, n) - g^D(k, m-1, n)] \} \otimes J_2^D(k, m, n) \end{aligned} \quad (13)$$

where the finite-difference method is used for the smooth approximation of the dyadic Green's function.

The computations of the discrete convolutions can be performed efficiently by means of cyclic convolutions and fast Fourier transform (FFT) [23], which is similar to the DDA method. As a traditional iterative solver of the resulting VIE matrix equation, the conjugate-gradient method converges very slowly and will produce the non-physical random errors in the calculation of optical absorption. To tackle the problem, we employ the fast and smoothly converging biconjugate gradient stabilized (BI-CGSTAB) method [24]. The FFT is adopted to accelerate the matrix-vector multiplications encountered in the BI-CGSTAB solver with computational complexity of $O(N \log N)$ and memory of $O(N)$.

Through the rigorous VIE solution to Maxwell's equations, we can access some important physical quantities to reveal the physical mechanism of plasmonic effects in OSCs and optimize device performances. The absorption spectrum of OSCs is calculated by

$$S_A(\lambda) = \int_V n_r(\lambda) k_i(\lambda) \frac{2\pi c_0}{\lambda} \epsilon_0 |\mathbf{E}|^2 dV \quad (14)$$

where $\mathbf{E} = \frac{\mathbf{J}}{-i_0 \omega (\epsilon - \epsilon_0)}$ is the total electric field, $n_c = n_r + i_0 k_i$ is the complex refractive index of the active material, λ is the incident wavelength, and c_0 is the speed of light in free space. It is worth mentioning that the absorption of various concentrators (involving single metallic cavity, single nanosphere, or plasmonic hybrid system) should be precluded in the volume integral above. A spectral enhancement factor (SEF) is the absorption spectrum of the OSC incorporating concentrators over that excluding concentrators. Integrating with a standard solar irradiance spectrum (air mass 1.5 global), one can get the total absorption of OSCs

$$T_A = \int_{400\text{nm}}^{800\text{nm}} S_A(\lambda) \Gamma(\lambda) d\lambda \quad (15)$$

where Γ is the solar irradiance spectrum. Likewise, a total enhancement factor (TEF) is the total absorption of the OSC incorporating concentrators over that excluding concentrators. To understand the mode hybridization for plasmon coupling, the polarization charge distribution on the surface of metallic nanostructure is given as follows

$$\rho_p = \nabla \cdot (\epsilon_0 \mathbf{E}) = -\nabla \cdot \mathbf{P} \quad (16)$$

where $\mathbf{P} = (\epsilon - \epsilon_0) \mathbf{E}$ is the polarization density. Based on the divergence-free condition, the polarization charge is definitely zero except on the heterogeneous boundaries. From the VIE solution, one can obtain the polarization current \mathbf{J} and the total electric field \mathbf{E} . After a post-processing procedure with Eqs. (14) and (15), the SEF and TEF can be easily accessible. In addition, both the two layered OSC structure and embedded concentrators are meshed by the volumetric cuboid cells with a uniform grid size of 1 nm.

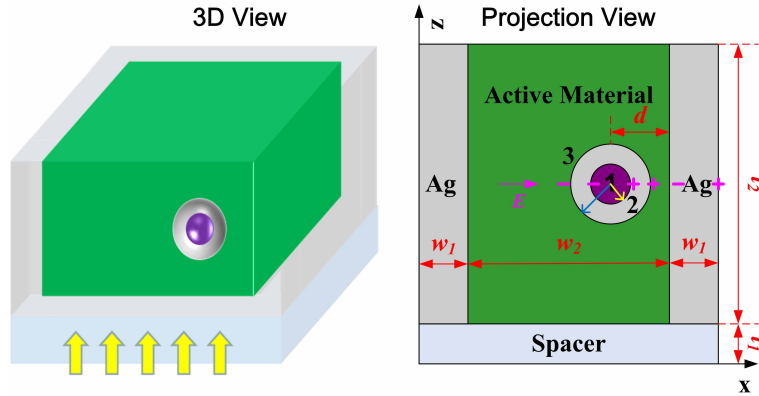


Fig. 1. (Color online) The schematic pattern of a heterojunction OSC. A hybrid plasmonic system, which comprises a plasmonic cavity coupled with a dielectric core-metal shell nanoparticle, is employed for improving the optical absorption of the active polymer material. A transparent spacer is inserted to avoid local shunt and extract carriers. The structural parameters are $t_1 = 20$ nm, $t_2 = 60$ nm, $w_1 = 30$ nm, $w_2 = 90$ nm, and $d = 21$ nm. The radius of the core layer (denoted by the yellow arrow) and that of the shell layer (denoted by the blue arrow) are set to $r_1 = 7.5$ nm and $r_2 = 15$ nm, respectively. For a bonding coupling mode in the hybrid system, the polarity of its polarization charge is also marked.

3. Results and Discussions

Figure 1 shows the schematic pattern of a heterojunction OSC. A hybrid plasmonic system, which comprises a plasmonic cavity coupled with a dielectric core-metal shell nanoparticle, is employed for improving the optical absorption of the active polymer material. A transparent spacer is inserted to avoid local shunt and extract carriers. The incident light is propagated from the spacer to the active layer at the vertical incident angle with an E -field polarized along the x direction. Figure 2(a) shows the real and imaginary parts of the refractive index of the active material measured from ellipsometry [25]. The complex refractive index of metal silver can be expressed by the Brendel-Bormann model [26]. The SiO_2 as a dielectric layer is adopted for the core-shell sphere and its refractive index can be found in the literature [27].

First, various nanoparticle concentrators (excluding the plasmonic cavity) are systematically and comparatively observed. These nanoparticles include a dielectric sphere, a metal sphere, a metal core-dielectric shell (MC-DS) sphere, and a dielectric core-metal shell (DC-MS) sphere [28]. The scattering cross section (SCS) of the nanoparticles can be obtained from the generalized reflection coefficients of the spherically layered media [29, 30]

$$\sigma_s = \frac{2\pi}{K_3^2} \sum_{m=1}^{\infty} (2m+1) \left(|\tilde{R}_{3,2}^{\text{TM}}(m)|^2 + |\tilde{R}_{3,2}^{\text{TE}}(m)|^2 \right) \quad (17)$$

where 1, 2, and 3 denote the core, shell, and active layers as shown in Fig. 1, respectively, m is the order of the modified spherical Bessel (Hankel) functions, and $\tilde{R}_{3,2}^{\text{TM}}$ and $\tilde{R}_{3,2}^{\text{TE}}$ are the generalized reflection coefficients of the TM and TE spherical waves in the layer 3 reflected by the layer 2. For small spherical particles, the leading term ($m = 1$) of $\tilde{R}_{3,2}^{\text{TM}}$ determines the value of the SCS. The generalized reflection coefficient can be written as a recursive equation

$$\tilde{R}_{i,i-1}^{\text{TM}} = R_{i,i-1}^{\text{TM}} + \frac{T_{i-1,i}^{\text{TM}} \tilde{R}_{i-1,i-2}^{\text{TM}} T_{i,i-1}^{\text{TM}}}{1 - R_{i-1,i}^{\text{TM}} \tilde{R}_{i-1,i-2}^{\text{TM}}} \quad (18)$$

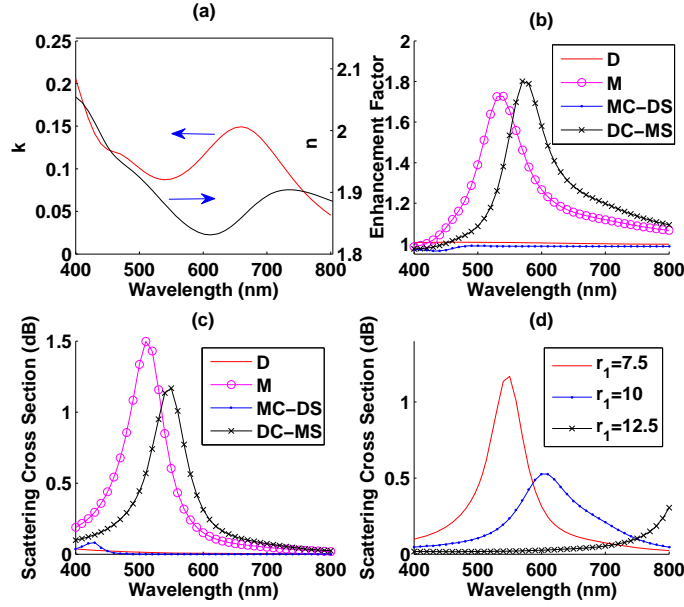


Fig. 2. (Color online) (a) The real and imaginary parts of the refractive index of the active material; (b) The spectral enhancement factors for various nanospheres. D denotes the dielectric sphere ($n=4$, $k=0$), M denotes the metal silver sphere, MC-DS denotes the metal core-dielectric shell sphere, and DC-MS denotes the dielectric core-metal shell sphere. The SiO_2 and Ag as a dielectric and metal layers are adopted for the core-shell spheres; (c) The scattering cross section (SCS) normalized to the geometrical cross section of each nanosphere; (d) The SCS of the DC-MS sphere as a function of the core radius (nm).

and

$$R_{i,i+1}^{\text{TM}} = \frac{\sqrt{\varepsilon_{i+1}\mu_i}\hat{H}_m^{(1)}(K_{i+1}r_i)\hat{H}_m^{(1)'}(K_i r_i) - \sqrt{\varepsilon_i\mu_{i+1}}\hat{H}_m^{(1)'}(K_{i+1}r_i)\hat{H}_m^{(1)}(K_i r_i)}{\sqrt{\varepsilon_i\mu_{i+1}}\hat{J}_m(K_i r_i)\hat{H}_m^{(1)'}(K_{i+1}r_i) - \sqrt{\varepsilon_{i+1}\mu_i}\hat{H}_m^{(1)}(K_{i+1}r_i)\hat{J}_m(K_i r_i)} \quad (19)$$

$$T_{i,i+1}^{\text{TM}} = \frac{i_0\varepsilon_{i+1}\sqrt{\mu_{i+1}/\varepsilon_i}}{\sqrt{\varepsilon_i\mu_{i+1}}\hat{J}_m(K_i r_i)\hat{H}_m^{(1)'}(K_{i+1}r_i) - \sqrt{\varepsilon_{i+1}\mu_i}\hat{H}_m^{(1)}(K_{i+1}r_i)\hat{J}_m(K_i r_i)} \quad (20)$$

$$R_{i,i-1}^{\text{TM}} = \frac{\sqrt{\varepsilon_i\mu_{i-1}}\hat{J}_m(K_i r_{i-1})\hat{J}_m'(K_{i-1}r_{i-1}) - \sqrt{\varepsilon_{i-1}\mu_i}\hat{J}_m'(K_i r_{i-1})\hat{J}_m(K_{i-1}r_{i-1})}{\sqrt{\varepsilon_{i-1}\mu_i}\hat{J}_m(K_{i-1}r_{i-1})\hat{H}_m^{(1)'}(K_i r_{i-1}) - \sqrt{\varepsilon_i\mu_{i-1}}\hat{H}_m^{(1)}(K_i r_{i-1})\hat{J}_m'(K_{i-1}r_{i-1})} \quad (21)$$

$$T_{i,i-1}^{\text{TM}} = \frac{i_0\varepsilon_{i-1}\sqrt{\mu_{i-1}/\varepsilon_i}}{\sqrt{\varepsilon_{i-1}\mu_i}\hat{J}_m(K_{i-1}r_{i-1})\hat{H}_m^{(1)'}(K_i r_{i-1}) - \sqrt{\varepsilon_i\mu_{i-1}}\hat{H}_m^{(1)}(K_i r_{i-1})\hat{J}_m'(K_{i-1}r_{i-1})} \quad (22)$$

where r_i , ε_i , μ_i , and K_i are the radius, permittivity, permeability, and wave number of the i th spherical layer, respectively. Figure 2(b) and 2(c) show the SEFs and the SCS of the nanospheres, respectively. As seen in Figs. 2(b) and 2(c), the peaks of the SEFs agree with those of the SCS well. The small dielectric nanosphere, although has no loss and large refractive index ($n=4$), is not a good concentrator for OSCs. The dielectric nanosphere with positive refractive index cannot produce a strong dipole resonance compared to the metal nanosphere. Moreover, in contrast to the DC-MS sphere that has a metal layer adjacent to different materials (SiO_2 and polymer), the resonance of the MC-DS sphere is blue-shifted because only

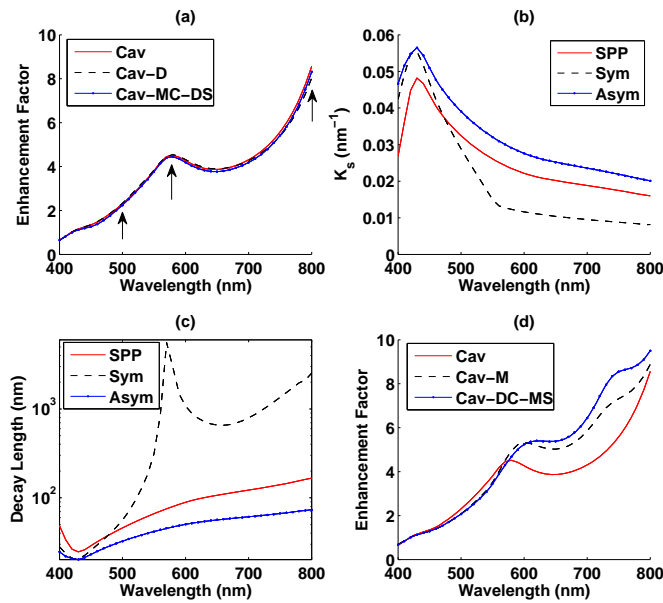


Fig. 3. (Color online) (a) The spectral enhancement factor (SEF) for the plasmonic cavity (Cav) and for that coupled with the dielectric (D) or the metal-core dielectric-shell (MC-DS) sphere; (b) The dispersion relations of surface plasmon polariton (SPP), and a symmetric (Sym) and asymmetric (Asym) surface wave modes. The surface plasmon polariton propagates at the interface between semi-infinite polymer and Ag half-spaces. The symmetric and asymmetric modes propagate in the active polymer layer bounded between the two metal claddings with finite thicknesses; (c) The decay lengths penetrated into the active material; (d) The SEFs for the plasmonic cavity and for that coupled with the metal (M) or the dielectric-core metal-shell (DC-MS) sphere.

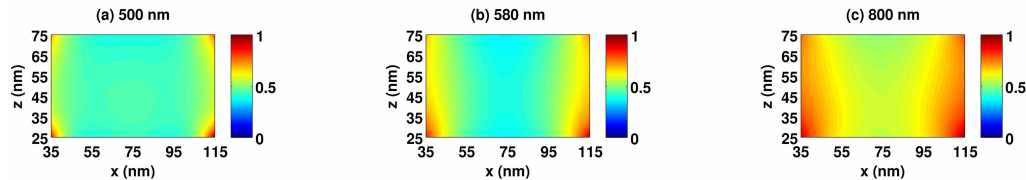


Fig. 4. (Color online) The near-field distributions in the active polymer layer at the wavelengths denoted with the arrows of Fig. 3(a). (a) 500 nm; (b) 580 nm; (c) 800 nm.

one material SiO_2 with lower refractive index is adjacent to the metal layer. The near field of the MC-DS sphere confines to the shell layer and cannot sufficiently scatter to the active layer. As a result, the optical enhancement by the MC-DS sphere is very weak. Figure 2(d) shows a tunable plasmon resonance by engineering the geometry of the DC-MS sphere. The resonance is red-shifted and becomes damped as the core radius increases.

Second, we investigate the plasmonic silver cavity structure enclosing the active polymer material. Here the nanosphere is excluded. Figure 3(a) shows the SEF by the plasmonic cavity. A broadband enhancement has a good overlap with the absorption spectrum of the active material as depicted in Fig. 1(a). The dispersion relation of the cavity resonator plays a key role in unveiling the fundamental physics of the significant optical enhancement. Different from

previous works assuming infinitely thick metal claddings [31], we take into account the finite-thickness effect of the metal claddings. The governing equation for an 1D eigenvalue problem of the Air/Ag/polymer/Ag/Air planar layered media is given by [29]

$$\left[p \frac{d}{dx} p^{-1} \frac{d}{dx} + K^2(x) \right] \phi(x) = K_z^2 \phi(x) \quad (23)$$

where $p = \varepsilon$ and $\phi = H_y$ for TM wave, and $p = \mu$ and $\phi = E_y$ for TE wave. The eigenvalue equation [Eq. (23)] can be easily solved by the finite-difference method [4] with perfectly matched layer absorbing boundary conditions [32, 33]. We find two eigenvalues of the TM wave closest to the momentum of surface plasmon polariton (SPP). The SPP propagates at the interface between semi-infinite polymer and Ag half-spaces and its dispersion relation is of the form

$$K_s = K_0 \sqrt{\frac{\varepsilon_{Ag} \varepsilon_{pol}}{\varepsilon_{Ag} + \varepsilon_{pol}}} \quad (24)$$

Particularly, the eigenvalue pair essentially corresponds to the symmetric and asymmetric surface wave modes supported by the Ag/polymer/Ag system [31]. These modes also are associated with the guided-wave poles of the generalized reflection coefficient for the planar layered media [29]. Figure 3(b) shows the dispersion relations. At long wavelengths, the dispersion relation of the SPP is located between those of symmetric and asymmetric modes. Then we calculate the decay lengths of the surface plasmon waves penetrated into the active material as plotted in Fig. 3(c). The peaks of the decay length of the symmetric mode strongly coincide with those of the SEF as shown in Fig. 3(a). The incident light excites symmetric surface plasmon waves at the bottom corners of the cavity and the waves propagate in the active layer bounded between the metal claddings. A short decay length away from the metal claddings makes E -fields concentrate at the surfaces of the metals. Contrarily, a long decay length induces a concentrated E -field in the center of the active material. Figure 4 demonstrates the near-field distributions in the active layer at the wavelengths denoted with the arrows of Fig. 3(a). At 800 nm, the slowly decaying near field away from the metal claddings leads to the most significant enhancement.

Third, we study the hybrid plasmonic system, which comprises a plasmonic cavity coupled with a nanosphere. The optical enhancement shows little improvements when the cavity is coupled with the dielectric or MC-DS sphere as illustrated in Fig. 3(a). However, a significant enhancement can be achieved if the cavity is coupled with metal or DC-MS sphere as shown in Fig. 3(d). By evaluating the TEF with the aid of Eq. (15), the optical absorption of the active polymer material has a four-fold increase when the cavity is coupled with the DC-MS sphere. We calculate the algebraic summation of the SEF by the uncoupled single cavity and that by the uncoupled single DC-MS sphere. As shown in Fig. 5, the summation is observably smaller than the SEF by the cavity coupled with the DC-MS sphere at long wavelengths ranging from 620 nm to 800 nm. The coherent interplay between the cavity and the DC-MS sphere is undoubtedly confirmed by the result. Then, we analyze the metal dissipation ratio defined as the metal loss of the coupled concentrator over that of the uncoupled one. The inset of Fig. 5 shows that the metal dissipation ratio of the DC-MS sphere is substantially larger than that of the cavity. The evanescent SPPs from the inner surface of metallic cavity sufficiently penetrate the DC-MS sphere inducing stronger local plasmon resonance as well as larger metallic loss. Thus the DC-MS sphere becomes more effective concentrator when it is coupled with the cavity. Finally, we discuss the coupling modes in the hybrid plasmonic system. Figure 6 depicts a polarization charge distribution on the surface of the cavity by using Eq. (16), indicating a bonding and antibonding coupling modes in the hybrid system. The bonding modes at 620 nm

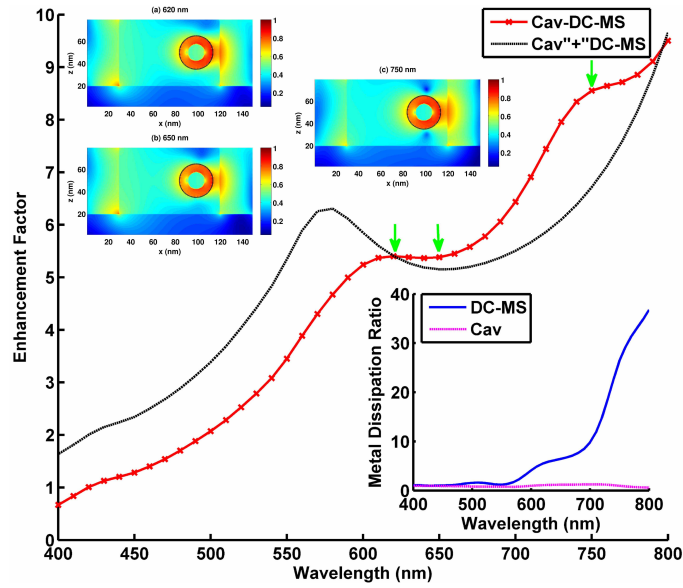


Fig. 5. (Color online) The spectral enhancement factor (SEF) comparisons. The SEF by the cavity (Cav) coupled with the dielectric core-metal shell (DC-MS) sphere is drawn with red straight line. The algebraic summation of the SEF by the uncoupled single cavity and that by the uncoupled single DC-MS sphere is plotted with black dash line. The near-field distributions at the wavelengths denoted with the green arrows are shown in the inset on a logarithmic scale. The metal dissipation ratio of the cavity is defined as the metal loss of the coupled cavity over that of the uncoupled one. Likewise, the metal dissipation ratio of the DC-MS sphere is defined as the metal loss of the coupled DC-MS sphere over that of the uncoupled one.

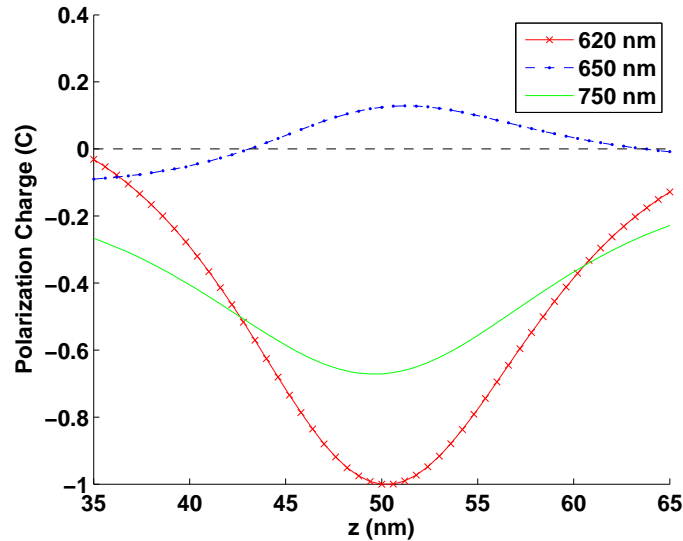


Fig. 6. (Color online) The polarization charge distributions on the surface of the cavity at the wavelengths denoted with the arrows of Fig. 5.

and 750 nm have a denser charge distribution if the distance between the cavity and the shell surfaces becomes closer. However, the antibonding mode at 650 nm reverses the polarity of the polarization charge when the face-to-face distance approaches the minimum. The near fields of the bonding modes show more concentrated field at the gap between the DC-MS sphere and the cavity, which can be seen in the inset of Fig. 5. For the bonding mode, the polarity of its polarization charge is marked in Fig. 1. Due to the in-phase plasmon oscillation and hybridization, the bonding mode is superradiant or strongly radiative, and provides a great help for the optical enhancement.

4. Conclusion

The hybrid plasmonic system, which comprises the plasmonic cavity coupled with the DC-MS nanosphere, can increase the optical absorption of the OSC by four fold. The significant enhancement mainly results from the coupling of symmetric surface wave modes supported by the cavity resonator and strongly depends on the decay length of surface plasmon waves penetrated into the active layer. Furthermore, the coherent interplay between the cavity and the DC-MS nanosphere is strongly demonstrated by our theoretical model. The bonding coupling mode in the hybrid plasmonic system enhances the optical absorption further. The work provides detailed physical explanations for the hybrid plasmonic cavity device structure to enhance the optical absorption of organic photovoltaics.

Acknowledgments

The authors acknowledge the support of the Research Grant Council of the Hong Kong Special Administrative Region, China (grants No. 712108, No. 711508, and No. 711609). This project is also supported in part by a Hong Kong UGC Special Equipment Grant (SEG HKU09).